Research article

# Transition metal elements-doped $SnO_2$ for ultrasensitive and rapid ppb-level formaldehyde sensing

Zejun Han [a,1], Yunxiang Tang [a,1], Guixia Lu [b,**], Yuan Qi [a], Hao Wu [c], Zhengyi Yang [a], Hecheng Han [a], Xue Zhang [a], Lili Wu [a,***], Zhou Wang [a], Jiurong Liu [a,****], Fenglong Wang [a,d,*]

[a] Key Laboratory for Liquid-Solid Structural Evolution and Processing of Materials Ministry of Education, Shandong University, Jinan, Shandong 250061, China
[b] School of Civil Engineering, Qingdao University of Technology, Qingdao, Shandong 266033, China
[c] School of Energy and Environment, City University of Hong Kong, Hong Kong, China
[d] Shenzhen Research Institute of Shandong University, A301 Virtual University Park in South District of Nanshan High-tech Zone, Shenzhen, China

A B S T R A C T

Pristine $SnO_2$, Fe-doped $SnO_2$ and Ni-doped $SnO_2$ were synthesized using facile hydrothermal method. Analysis based on XRD, TEM and UV–Vis DRS measurements demonstrated the successful insertion of Fe and Ni dopants into $SnO_2$ crystal. Formaldehyde-detection measurements revealed that transition metal-doped $SnO_2$ exhibited improved formaldehyde-sensing properties compared with that of pristine $SnO_2$. When the amount of incorporated dopant (Fe or Ni) was 4 at.%, the most effective enhancement on sensing performance of $SnO_2$ was obtained. At 160 °C, the 4 at.% Fe–$SnO_2$ and 4 at.% Ni–$SnO_2$ exhibited higher response values of 7.52 and 4.37 with exposure to low-concentration formaldehyde, respectively, which were 2.4 and 1.4 times higher than that of pristine $SnO_2$. The change of electronic structure and crystal structure as well as catalytic effect of transition metals are chiefly responsible for the enhanced sensing properties.

## 1. Introduction

Formaldehyde as a toxic and polluted gas that is mainly released indoors from the widely-applied building and decorating materials [1–7]. Researches have demonstrated that long-term exposure to formaldehyde vapor may cause a series of health problems including lung damage, immune system disorders, allergic dermatitis, and cancer [8–10]. Many associations have issued formaldehyde warnings to people [9]. The World Health Organization (WHO) stipulates that a safe concentration of formaldehyde vapor for human exposure over a long time without exceeding approximately 0.08 ppm [3,11,12]. However, concentrations of gaseous formaldehyde are relatively low, and thus difficult to detect and highly challenging to quantify. As a consequence, developing techniques that enable to

---

* Corresponding author. Key Laboratory for Liquid-Solid Structural Evolution and Processing of Materials Ministry of Education, Shandong University, Jinan, Shandong 250061, China.
** Corresponding author.
*** Corresponding author.
**** Corresponding author.
*E-mail addresses:* lgxia1988@163.com (G. Lu), wulili@sdu.edu.cn (L. Wu), jrliu@sdu.edu.cn (J. Liu), fenglong.wang@sdu.edu.cn (F. Wang).
[1] These authors contributed equally to this work.

detection of trace formaldehyde selectively and immediately is significantly urgent.

Over the last few years, a series of metal oxide semiconductors (MOSs) for formaldehyde detection have been reported, such as $SnO_2$ [13], ZnO, $In_2O_3$ [14], NiO [15] and $Fe_2O_3$ [16]. [3,17–19]. Although it has been proved that MOSs are competent in detecting formaldehyde, the high operating temperature, inferior selectivity, long-time response and recovery, as well as ineffective sensitivity towards tracing formaldehyde gravely obstruct their further widespread applications [8,20,21]. Therefore, how to effectively ameliorate their formaldehyde-sensing performance is heavily imperative.

Considerable efforts have already been essayed to improve the gas sensing performance of MOSs. Surface modification with noble metals including aurum (Au), silver (Ag), platinum (Pt) and palladium (Pd) is regarded as an efficient-enhancing approach because of their remarkable catalytic effect in sensing processes [22–29]. However, the extremely expensive cost owing to their scarce reserve is specifically inappropriate for commercialization [30–34]. In addition, element doping is considered to be a favorable alternative method, which alters the electronic properties of MOSs and stimulates more gas molecule adsorption sites in turn leads to a positive influence on the gas sensing performances [35–37]. Wang et al. prepared Co-doped $In_2O_3$ and a lower operating temperature was obtained compared with that of pristine $In_2O_3$ [38]. Han et al. compared the pristine $In_2O_3$ and Ce-doped $In_2O_3$ and an enhanced sensing performance towards methanol were observed in Ce-doped $In_2O_3$ [39]. Wu's group inserted Al dopant into $SnO_2$ and ameliorated its ability to detect formaldehyde [40]. Lin et al. enhanced the sensing performance of $SnO_2$ to formaldehyde by Ni doping [41]. The Ni-incorporated $SnO_2$ exhibited an extremely high-speed response of 6 s at 100 °C towards 100 ppm formaldehyde. Hu et al. also verified that $SnO_2$ with Ni dopant performed better in tracing formaldehyde in comparison with pure $SnO_2$ [42]. Zhu and his co-workers introduced yttrium (Y) into $SnO_2$ [43]. At the working temperature of 180 °C, the response and recovery time of Y-inserted $SnO_2$ exposed to 25 ppm formaldehyde were 8 s and 10 s, respectively. In these studies, firstly, the existence of heteroatoms promotes the generation of defects such as oxygen vacancies which are beneficial to the formation of chemisorbed oxygen species, thus effectively improving the sensing performance of original oxides [44,45]. Secondly, the introduction of dopants can affect the size of the pristine-crystal structure, which may result in higher specific surface areas and thereby enhance the sensing properties [39,46]. Thirdly, expected as effective catalysts, transition metals such as Fe, Co and Ni enable to promote the chemical reactions occurring on the surface efficiently [46–48]. Yet, metal-doped MOSs are still suffering from high working temperatures, weak selectivity, and especially unsatisfying sensitivity to low-concentration formaldehyde.

In this study, Fe-doped $SnO_2$ and Ni-doped $SnO_2$ were prepared via a simple hydrothermal method. By adjusting the quantity of dopant that adulterated into $SnO_2$, we found that when the amount of Fe and Ni element was 4 at.%, the insertion of heteroatoms effectively enhance the formaldehyde-tracking ability of pristine $SnO_2$, especially towards the low-concentration formaldehyde, which shows great potential in the future. In addition, the mechanism of improved sensing performances was discussed.

## 2. Experimental section

All chemical reagents supported by Sinopharm Chemical Reagent Co., Ltd were analytical grade without any further purification to utilize, including tin (IV) chloride pentahydrate ($SnCl_4·5H_2O$), ferric (III) nitrate nonahydrate ($Fe(NO_3)_3·9H_2O$), nickel (II) chloride hexahydrate puratrem ($NiCl_2·6H_2O$), sodium hydroxide (NaOH) and ethanol ($CH_3CH_2OH$).

### 2.1. Preparation of sensing materials

#### 2.1.1. Synthesis of $SnO_2$

The preparation of $SnO_2$ was achieved concisely via the hydrothermal method. Firstly, $SnCl_4·5H_2O$ and NaOH at a molar ratio of 1:7 were dissolved into 30 mL of deionized water and the mixture was fiercely stirred for approximately 30 min. Subsequently, the homogeneous solution sealed in Teflon-lined stainless steel autoclave was maintained at 180 °C for 16 h. Finally, the white sediment collected by centrifugation with deionized water washing was dried in the oven.

#### 2.1.2. Synthesis of Fe-doped $SnO_2$

The fabrication of Fe-doped $SnO_2$ was similar to that of $SnO_2$. In a specific procedure, $SnCl_4·5H_2O$ and NaOH at a molar ratio of 1:7 were dissolved into 30 mL of deionized water. Then a certain amount of $Fe(NO_3)_3·9H_2O$ was added and the mixture was stirred drastically for about 30 min. Afterward, the homogeneous solution was sealed in Teflon-lined stainless steel autoclave and kept at 180 °C for 16 h. Ultimately, the product was collected via centrifuging sediment with deionized water washing followed by drying in the oven. Controlling the amount of $Fe(NO_3)_3·9H_2O$ added, a series of samples were obtained, which were marked as 2 at.% Fe–$SnO_2$, 4 at.% Fe–$SnO_2$, 6 at.% Fe–$SnO_2$ and 8 at.% Fe–$SnO_2$.

#### 2.1.3. Synthesis of Ni-doped $SnO_2$

The fabrication of Ni-doped $SnO_2$ was similar to that of $SnO_2$. In a typical process, $SnCl_4·5H_2O$ and NaOH at a molar ratio of 1:7 were dissolved into 30 mL of deionized water. Then a certain amount of $NiCl_2·6H_2O$ was added, after which the mixture was stirred vigorously for about 30 min. Then the homogeneous solution was transferred into Teflon-lined stainless steel autoclave and retained at 180 °C for 16 h. Eventually, the sediment was collected via centrifugation with deionized water washing and then dried in the oven. The samples, named as 2 at.% Ni–$SnO_2$, 4 at.% Ni–$SnO_2$, 6 at.% Ni–$SnO_2$ and 8 at.% Ni–$SnO_2$, were gained via regulating the quantity of $NiCl_2·6H_2O$ used.

## 2.2. Characterizations

Analysis of the crystal structure of as-prepared samples was conducted with the help of X-ray diffraction (XRD, DMAX–2500PC) using Cu-Kα radiation ($\lambda = 1.542$ Å). The scanning rate was assigned as $10°$ $min^{-1}$ with the scanning scope from $10°$ to $90°$. Based on Scanning electron microscopy (SEM, SU–70) with an accelerating voltage of 15 kV, morphology and nanostructure of as-synthesized samples were verified. Detailed analysis of the surface structure of the as-synthesized samples was established on the transmission electron microscopy (TEM) operated on a JEM–1011 instrument and high-resolution transmission electron microscopy (HRTEM) manipulated on a JEM–2100 instrument, during which the accelerating voltage was maintained at 100 and 200 kV, respectively. X-ray photoelectron spectrometer (XPS) based on an AXIS Supra instrument with a monochromatic Al–Kα radiation ($h\upsilon = 1486.6$ eV) was carried out to figure out the surface chemical states, after which the energy value of 284.6 eV was accepted as the indefinite C 1s line to rectify the binding energy. UV–visible diffuse reflectance spectrum (UV–Vis DRS) was manipulated on a UV–3600i Plus to affirm the electronic structure of the synthesized samples.

## 2.3. Gas-sensing measurements

The formaldehyde-sensing sensor was manufactured by coating a layer of thin film on the $Al_2O_3$-based substrate with the sensing-material slurry repeatedly smeared on it. The sensing performance of as-prepared samples towards formaldehyde was confirmed built on the gas-sensitivity experiment performed on a WS–30A instrument (Zhengzhou Winsen Electronics Co., Ltd., Henan, China) at the environmental temperature of 25 °C without air humidity surpassing 20%. A detailed description could be found in our previous work [2]. The response and recovery time is appointed as the time experienced for a sensor to reach 90% of the complete resistance change subsequent to gas input or emission [49,50].

## 3. Results and discussion

### 3.1. Structural and morphological characteristics

XRD patterns of Fe-incorporated $SnO_2$ and Ni-incorporated $SnO_2$ are illustrated in Fig. 1. It can be determined that all characteristic diffraction peaks of prepared samples are coincident with the tetragonal phase of $SnO_2$ (JCPDS–77–0449). Characteristic peaks associated with other phases are inexistent, which signifies the ultra-low amount of iron oxides and nickel oxides. Besides, in comparison with pristine $SnO_2$, the right shift of characteristic diffraction peaks was observed in Fe-doped $SnO_2$ (Fig. 1a) and Ni-doped $SnO_2$ (Fig. 1b) and this indicates a shrinkage of $SnO_2$ lattice, resulting from the insertion of dopants. To investigate changes of the crystal structures, Rietveld refinements of pristine $SnO_2$, Fe-doped $SnO_2$ and Ni-doped $SnO_2$ were performed (Fig. S1), and the detailed structure refinement parameters are shown in Table S1. The results reveal that the lattice constants of $SnO_2$ become smaller after Fe and Ni doping. It is highly believed that the change of lattice structure is conducive to strengthening the gas-detection capability of MOSs [51–53].

SEM images of pristine $SnO_2$, 2 at.% Fe–$SnO_2$, 4 at.% Fe–$SnO_2$, 6 at.% Fe–$SnO_2$, 8 at.% Fe–$SnO_2$, 2 at.% Ni–$SnO_2$, 4 at.% Ni–$SnO_2$, 6 at.% Ni–$SnO_2$ and 8 at.% Ni–$SnO_2$ are shown in Fig. S2. The hollow sphere-like morphology of pristine $SnO_2$ particles less than 2 μm is verified. In addition, reduced size of $SnO_2$ and damage on micromorphology due to the introduction of Fe and Ni dopants are also observed, in which an escalating tendency is manifested with increasing insertion of Fe and Ni elements.

TEM images of 4 at.% Fe–$SnO_2$ and 4 at.% Ni–$SnO_2$ are illustrated in Fig. 2 to show the micromorphology and structure of transition metal-inserted $SnO_2$. From Fig. 2a and c, it can be seen that both 4 at.% Fe–$SnO_2$ and 4 at.% Ni–$SnO_2$ are irregularly constructed by a raft of rods and their sizes are bigger than 500 nm but smaller than 2 μm. As illustrated in Fig. 2b and d, both of the lattice spacings of 4 at.% Fe–$SnO_2$ and 4 at.% Ni–$SnO_2$ are measured at approximately 0.319 nm, which corresponds to the (110) spacing of $SnO_2$. The lattice spacing of pristine $SnO_2$ (0.335 nm) is larger than those of transition metal-incorporated $SnO_2$, which is tightly connected with the shrinkage of $SnO_2$ crystal originating from the insertion of transition metals. The observation of TEM is concordant with those of XRD and SEM.
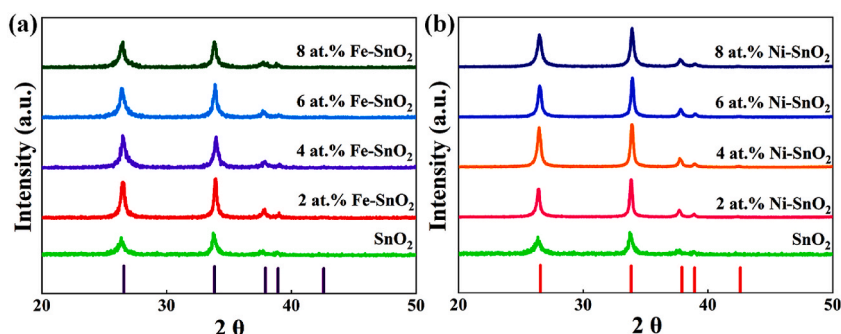


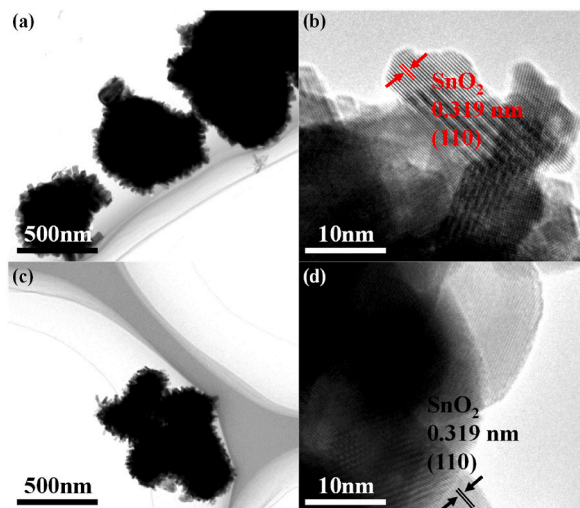**Fig. 1.** XRD patterns of (a) Fe-doped $SnO_2$ and (b) Ni-doped $SnO_2$.

**Fig. 2.** TEM images of (a)–(b) 4 at.% Fe–SnO$_2$ and (c)–(d) 4 at.% Ni–SnO$_2$ at different magnification.

XPS spectra of involved elements are depicted in Fig. 3. Fig. 3a shows the Sn 3d orbital spectrum. The intense peaks located at 486.56 eV and 494.93 eV in pristine SnO$_2$, 486.54 eV and 494.95 eV in 4 at.% Fe–SnO$_2$, as well as 486.59 eV and 494.86 eV in 4 at.% Ni–SnO$_2$ distinctly conform to Sn$^{4+}$ [13]. In the Fe 2p orbital spectrum illustrated in Fig. 3b, the characteristic peak at 712.22 eV is observed, which clearly corresponds to Fe$^{3+}$ [54–56]. The binding energies of Ni located at 855.95 eV and 873.41 eV are ascribed to Ni$^{2+}$ of Ni 2p$_{3/2}$ and Ni 2p$_{1/2}$, respectively (Fig. 3c) [57–59]. The O 1s orbital spectra of pristine SnO$_2$, 4 at.% Fe–SnO$_2$ and 4 at.% Ni–SnO$_2$ are exhibited in Fig. 3d–f. It is observed that each of them enables to be deconvoluted into two intense peaks. The apparent peaks, situated at 530.42 eV and 531.35 eV in pristine SnO$_2$, 530.39 eV and 531.27 eV in 4 at.% Fe–SnO$_2$ as well as 530.36 eV and 531.54 eV in 4 at.% Ni–SnO$_2$, are due to lattice oxygen and adsorbed oxygen species [3,60–62]. The inexistence of peaks related to oxygen vacancies can be possibly ascribed to their trace quantity.

To further verify the incorporation of heteroatoms into SnO$_2$ lattice, Analysis of the electronic structure in prepared samples was conducted through UV–Vis DRS. UV–visible absorption spectrum of Fe-doped SnO$_2$ illustrated in Fig. 4a demonstrates that the adsorption wavelength of Fe-incorporated SnO$_2$ is red-shifted compared with that of pristine SnO$_2$. A similar observation is also obtained in Ni-doped SnO$_2$, as described in Fig. 4b. These suggest that the electrons in transition metal-inserted SnO$_2$ need lower energy to cross the forbidden band in comparison with that of original SnO$_2$. From UV–visible absorption spectra, the correlation between
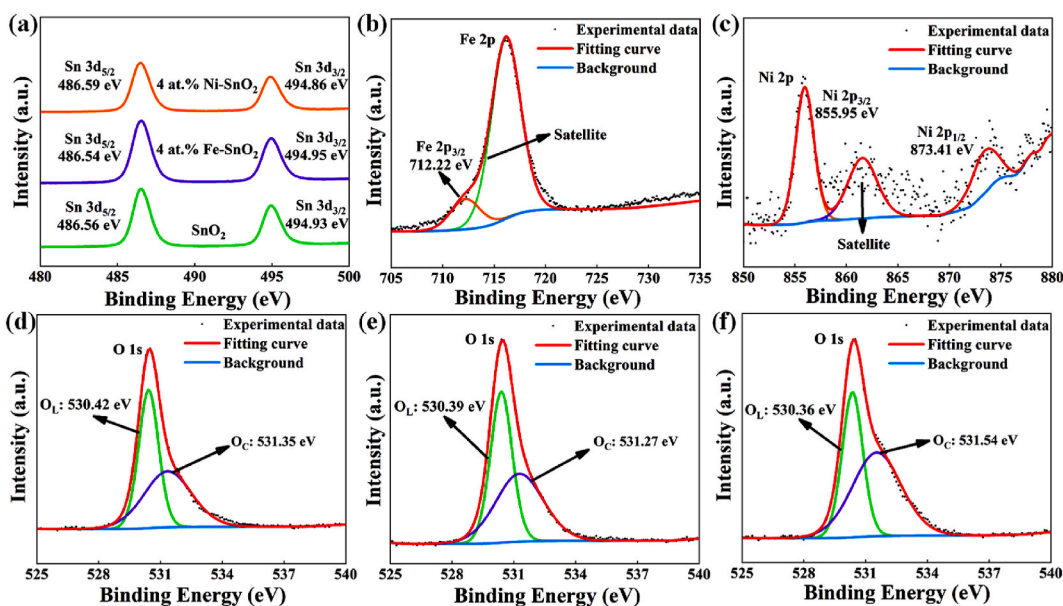


**Fig. 3.** XPS spectra of the (a) Sn 3d orbital, (b) Fe 2p orbital and (c) Ni 2p orbital; O 1s orbital of (d) pristine SnO$_2$, (e) 4 at.% Fe–SnO$_2$ and (f) 4 at.% Ni–SnO$_2$.
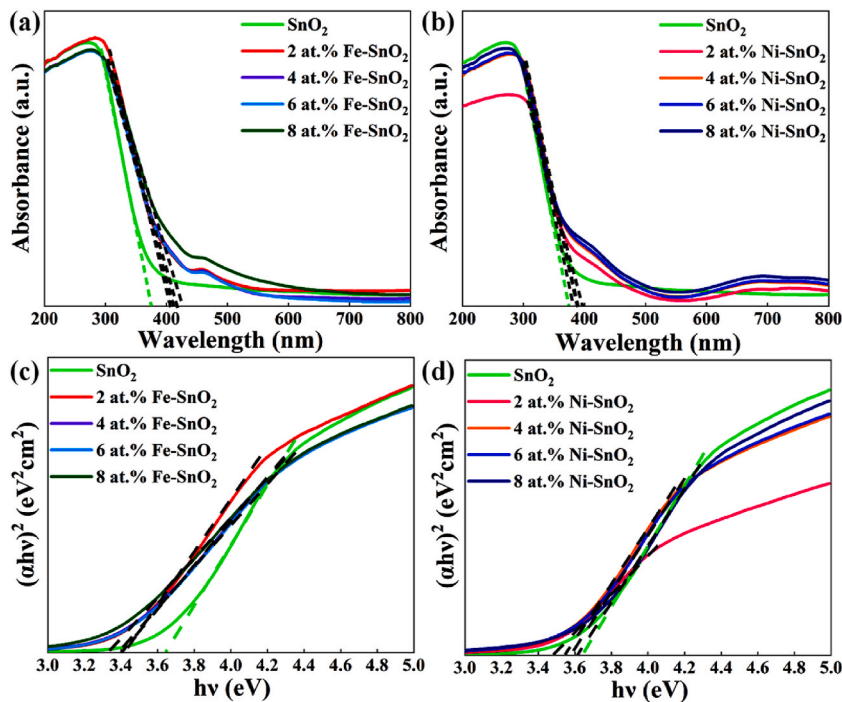
**Fig. 4.** UV–visible absorption spectra of (a) Fe-doped $SnO_2$ and (b) Ni-doped $SnO_2$; T-plots of $(\alpha h\nu)^2$ versus h$\nu$ of (c) Fe-doped $SnO_2$ and (d) Ni-doped $SnO_2$.

$(\alpha h\nu)^2$ and h$\nu$ in Fe-doped $SnO_2$ and Ni-doped $SnO_2$ was also gained, which is shown in Fig. 4c and d. A clear reduction of gap band occurs in both Fe-doped $SnO_2$ and Ni-doped $SnO_2$, certifying the narrowing forbidden band. The shrinkage of forbidden band is conducive to electronic transition, which can enlarge the electronic concentration in conduction band and then increase the amount of adsorbed oxygen species, thereby enhancing the formaldehyde-sensing performance [51].

### 3.2. Sensing properties towards formaldehyde

The optimal operating temperature of pristine $SnO_2$, Fe-incorporated $SnO_2$ and Ni-inserted $SnO_2$ was confirmed by comparing their response values exposed to 1 ppm formaldehyde at different temperatures. As illustrated in Fig. 5a, an obviously volcano-like correlation between response value and working temperature is obtained. Except 8 at.% Fe–$SnO_2$, the response values of all samples towards 1 ppm formaldehyde reach the maximum at 160 °C, among which 4 at.% Fe–$SnO_2$ exhibits the largest response value of approximately 7.52. For 8 at.% Fe–$SnO_2$, the temperature of 200 °C is the optimal operating temperature. However, due to the subtle differences in the response values observed at 160 °C and 200 °C, the optimal operating temperature of 8 at.% Fe–$SnO_2$ is also obtained at 160 °C. Therefore, the temperature of 160 °C is adopted as the optimal operating temperature and all sensing tests were conducted at this temperature. Fig. 5b demonstrates that, the response of Fe-doped $SnO_2$ and Ni-doped $SnO_2$ exposed to 1 ppm formaldehyde at
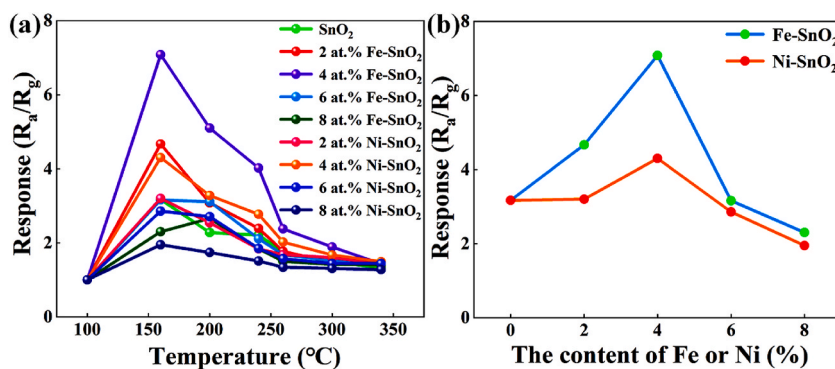


**Fig. 5.** (a) Response of pristine $SnO_2$, Fe-doped $SnO_2$ and Ni-doped $SnO_2$ towards 1 ppm formaldehyde at different temperatures; (b) Response of Fe-doped $SnO_2$ and Ni-doped $SnO_2$ with different proportions of dopant incorporated towards 1 ppm formaldehyde at 160 °C.

160 °C is distinctly intensified with the incorporation increasing until the amount reaches to 4 at.%, and then curbed completely with the insertion exceeding 4 at.%. Thus, 4 at.% is the best doping rate for $SnO_2$, at which Fe or Ni elements enable to ameliorate the formaldehyde-detection performance significantly. In addition, Table S2 briefly summarises the gas sensing performance of various MOSs based gas sensors toward formaldehyde. It is worth noting that the sensor fabricated in this work exhibits better sensing performance to 1 ppm formaldehyde at low working temperatures than those reported in the literature.

The response curves of 4 at.% Fe–$SnO_2$ and 4 at.% Ni–$SnO_2$ towards 1 ppm formaldehyde at 160 °C are displayed in Fig. 6a and b. Both 4 at.% Fe–$SnO_2$ and 4 at.% Ni–$SnO_2$ exhibit an evident response immediately after the formaldehyde gas input, and the response time of 4 at.% Fe–$SnO_2$ and 4 at.% Ni–$SnO_2$ is 42 s and 7 s, respectively. Afterward, with formaldehyde removed, they can recover to the original state, and a high-speed recovery time of 20 s is gained in 4 at.% Ni–$SnO_2$. Fig. 6c compares the response and recovery time of all Fe-doped $SnO_2$ towards 1 ppm formaldehyde at 160 °C. The response time of 4 at.% Fe–$SnO_2$ is the shortest among all involved samples, but its recovery time is a little long. 4 at.% Ni–$SnO_2$ is the fastest in both response and recovery, as depicted in Fig. 6d.

Fig. 7a suggests that, within 1 ppm formaldehyde, the ln[S] of 4 at.% Fe–SnO2 and 4 at.% Ni–SnO2 linearly correlates with the ln [C]. Fig. 7b and cFig. 7 exhibit four-time responses of 4 at.% Fe–SnO2 and 4 at.% Ni–SnO2 to 1 ppm formaldehyde at 160 °C, which proclaims excellent repeatability.

Considering practical applications, the ability to resist interfering gases is an essential aspect for evaluating the sensing properties [27,63]. Thus, anti-interference measurements based on various gases including methanol, ethanol, sulfur dioxide, nitrogen dioxide, ammonia, carbon monoxide and formaldehyde were implemented, as illustrated in Fig. 8a. There is no response of pristine $SnO_2$, 4 at. % Fe–$SnO_2$ and 4 at.% Ni–$SnO_2$ to sulfur dioxide, nitrogen dioxide, ammonia and carbon monoxide. Compared with pristine $SnO_2$, the selectivity of 4 at.% Fe–$SnO_2$ and 4 at.% Ni–$SnO_2$ towards formaldehyde is greatly enhanced. Meantime, an outstanding anti-interference capability towards methanol and ethanol is achieved by 4 at.% Fe–$SnO_2$. With a comprehensive comparison, 4 at.% Fe–$SnO_2$ is expected to be more selective to formaldehyde and more appropriate for real-world use. The mechanisms of selectivity are extremely intricate [64]. Formaldehyde molecules with a lower bond dissociation energy compared with that of other gases may take part in redox reaction preferentially [65,66]. Additionally, there is also consideration on differences in reaction process, adsorption capability and dipole moment [67–69]. Ultimately, the measurement of response towards 1 ppm formaldehyde within one month was carried out to determine the stability of sensing materials, which is showed in Fig. 8b. It can be clearly observed that the response of all measured materials virtually remains stable without big waves, expressing decent long-term stability. Low operating temperature and steady construction is likely responsible for good stability [70].

### 3.3. Sensing mechanisms

It is extensively acknowledged that the sensing performance of MOSs is heavily determined by the chemical reactions occurring on
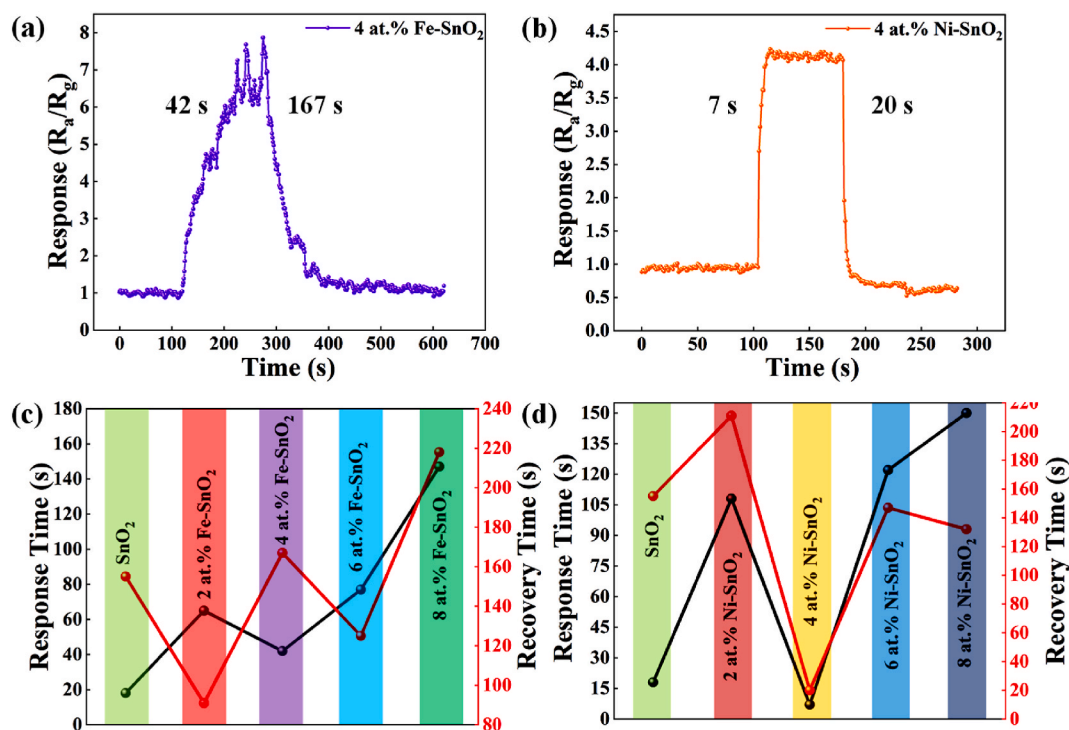


**Fig. 6.** Response curves of (a) 4 at.% Fe–$SnO_2$ and (b) 4 at.% Ni–$SnO_2$; Response and recovery time of (c) Fe-doped $SnO_2$ and (d) Ni-doped $SnO_2$ towards 1 ppm formaldehyde at 160 °C.
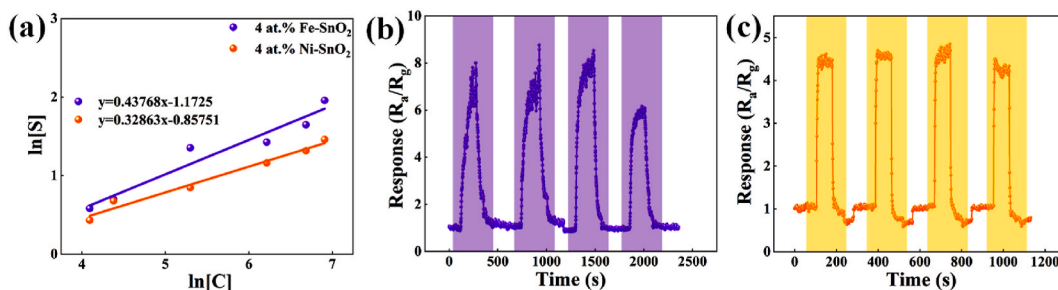
**Fig. 7.** (a) The linear fitting between ln[C] and ln[S] (C is the concentration of formaldehyde; S is the response value); The repeatability of (b) 4 at. % Fe–SnO$_2$ and (c) 4 at.% Ni–SnO$_2$ towards 1 ppm formaldehyde at 160 °C.
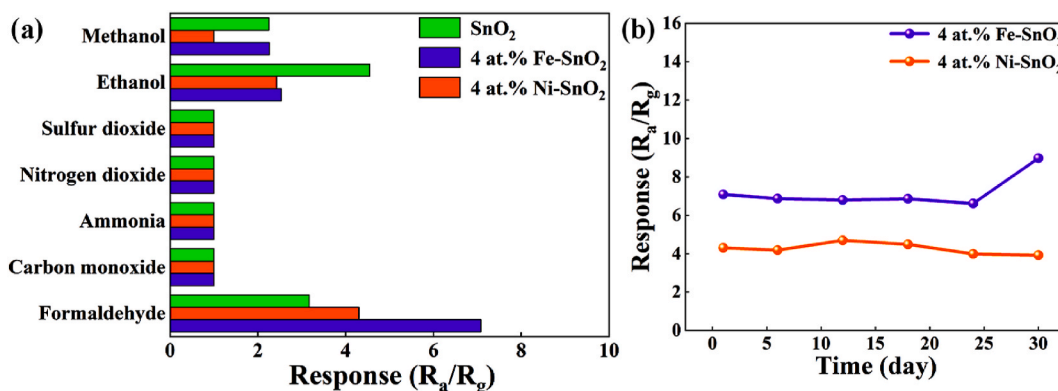


**Fig. 8.** (a) Response of pristine SnO$_2$, 4 at.% Fe–SnO$_2$ and 4 at.% Ni–SnO$_2$ towards 1 ppm interfering gases (The concentration of ethanol and methanol is 10 ppm, respectively); (b) The response of 4 at.% Fe–SnO$_2$ and 4 at.% Ni–SnO$_2$ towards 1 ppm formaldehyde in one month.

the surface [71]. The entire process is depicted in Fig. 9. First, oxygen molecules in atmosphere can be adsorbed on the surface of SnO$_2$ due to physical interactions [72]. These oxygen molecules enable to capture the conduction-band electrons in SnO$_2$ and form adsorbed oxygen species with high activity such as O$_2^-$, O$^-$, and O$^{2-}$ simultaneously, during which both of the thickness of electron depletion layer (EDL) and resistance of SnO$_2$ enlarge [65,73,74]. Afterward, when the SnO$_2$ is exposed to formaldehyde-surrounded ambience, redox reactions take place immediately between formaldehyde molecules and chemisorbed oxygen species (Fig. 9a). During this process, the generated electrons will be released back to the conduction band of SnO$_2$, thereby observing reduced thickness of EDL as well as resistance of sensing material [29,75]. The above-mentioned processes can be synoptically summarized as follows equations (1–8) [5,71,72,76].

$$O_2 \text{ (gas)} \rightarrow O_2 \text{ (ads)}, \tag{1}$$

$$O_2 \text{ (ads)} + e^- \rightarrow O_2^- \text{ (ads)}, \tag{2}$$

$$O_2^- \text{ (ads)} + e^- \rightarrow 2O^- \text{ (ads)}, \tag{3}$$

$$O^- \text{ (ads)} + e^- \rightarrow O^{2-} \text{ (ads)}, \tag{4}$$

$$HCHO \text{ (gas)} \rightarrow HCHO \text{ (ads)}, \tag{5}$$

$$HCHO \text{ (ads)} + 2O^- \text{ (ads)} \rightarrow CO_2 \text{ (gas)} + H_2O \text{ (gas)} + 2e^-, \tag{6}$$

$$HCHO \text{ (ads)} + O_2^- \text{ (ads)} \rightarrow CO_2 \text{ (gas)} + H_2O \text{ (gas)} + e^-, \tag{7}$$

$$HCHO \text{ (ads)} + 2O^{2-} \text{ (ads)} \rightarrow CO_2 \text{ (gas)} + H_2O \text{ (gas)} + 4e^-. \tag{8}$$

In this study, transition metal-incorporated SnO$_2$ performed better than pristine SnO$_2$ in tracing low-concentration formaldehyde. The enhancing mechanisms are illustrated in Fig. 9b. First, because of the differences between Sn and transition metal ions in electronegativity and ionic radius, lattice defects will be produced after adulteration. Therefore, the gap band of SnO$_2$ will narrow under the influence of Moss-Burstein effect [51], which has been verified by the observation from UV–Vis DRS. Obviously, this will make the electronic transition easier in comparison with pristine SnO$_2$, which is beneficial to the electronic-concentration enlargement in conduction band, thereby conducive to the formation of chemisorbed oxygen species [77]. Increased oxygen species enable to react
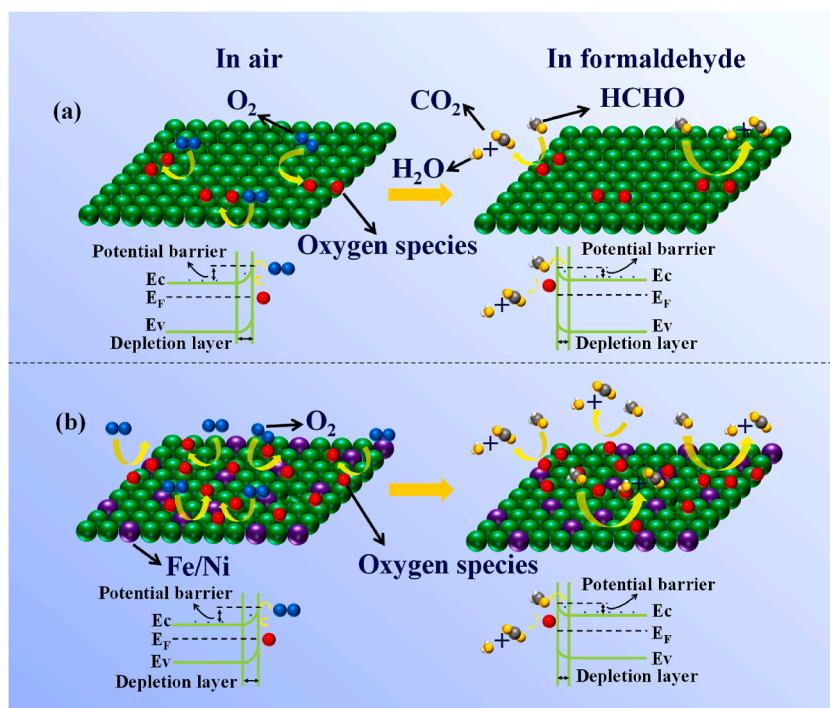
**Fig. 9.** Schematic of the formaldehyde-sensing mechanisms for (a) pristine $SnO_2$ and (b) Fe/Ni–$SnO_2$.

with more formaldehyde molecules. Second, the catalytic effect of Fe or Ni dopant contributes to the efficiency that formaldehyde molecules take part in the surface reaction, thus promoting sensitivity [47,51,78]. Third, in accordance with XRD spectra and SEM images, reduced size of crystal structure occurred, which may influence the adsorption of gas molecules [51].

## 4. Conclusion

In this study, pristine $SnO_2$, Fe-doped $SnO_2$ and Ni-doped $SnO_2$ were prepared through hydrothermal method. Analysis reveals that the incorporation of Fe or Ni results effectively-improved sensing properties of $SnO_2$ towards formaldehyde. Especially, at 160 °C, the response value of 4 at.% Fe–$SnO_2$ and 4 at.% Ni–$SnO_2$ exposed to 1 ppm formaldehyde is 7.52 and 4.37, respectively, higher than that of pristine $SnO_2$. Moreover, compared with the Ni-doped $SnO_2$, the higher response value over Fe-doped $SnO_2$ could be attributed to its narrower band gap, which more thermally excited carriers within it might be generated, and thus more adsorbed oxygen ions will be accumulated gathering in the surface of the materials. Meanwhile, the response time of 4 at.% Fe–$SnO_2$ and 4 at.% Ni–$SnO_2$ is only 42 s and 7 s, respectively. These observations demonstrate that insertion with transition metals such as Fe and Ni dopants is suitable for promoting the formaldehyde-sensing capability of original $SnO_2$, which is expected as a competitive and cost-effective strategy for detecting low-concentration formaldehyde. The enhancement can be mainly attributed to the change of electronic structure and crystal structure as well as the catalytic effect of transition metal.

## Author contribution statement

Zejun Han, Yunxiang Tang: Conceived and designed the experiments; Performed the experiments; Analyzed and interpreted the data; Wrote the paper.

Guixia Lu, Yuan Qi, Hao Wu, Zhengyi Yang, Hecheng Han, Xue Zhang: Analyzed and interpreted the data.

Lili Wu, Zhou Wang, Jiurong Liu, Fenglong Wang: Contributed reagents, materials, analysis tools or data.

## Funding statement

## Data availability statement

Data included in article/supp. material/referenced in article.

## Declaration of interest's statement

The authors declare no competing interests.

## Appendix A. Supplementary data

Supplementary data to this article can be found online at https://doi.org/10.1016/j.heliyon.2023.e13486.

## References

[1] Z. Han, Y. Tang, G. Lu, Y. Qi, H. Wu, Z. Yang, H. Han, X. Zhang, L. Wu, Z. Wang, J. Liu, F. Wang, PtCu-SnO₂ nanocomposites for ultrasensitive and rapid ultra-low formaldehyde sensing, ChemPhys Mater. 1 (3) (2022) 227–236, https://doi.org/10.1016/j.chphma.2022.03.007.

[2] Y. Tang, Z. Han, Y. Qi, Z. Yang, H. Han, Y. Jiang, X. Zhang, L. Wu, Z. Wang, J. Liu, F. Wang, Enhanced ppb-level formaldehyde sensing performance over Pt deposited SnO₂ nanospheres, J. Alloys Compd. 899 (2022), 163230, https://doi.org/10.1016/j.jallcom.2021.163230.

[3] R. Xu, L.-X. Zhang, M.-W. Li, Y.-Y. Yin, J. Yin, M.-Y. Zhu, J.-J. Chen, Y. Wang, L.-J. Bie, Ultrathin SnO₂ nanosheets with dominant high-energy {001} facets for low temperature formaldehyde gas sensor, Sens. Actuator B–Chem. 289 (2019) 186–194, https://doi.org/10.1016/j.snb.2019.03.012.

[4] H.J. Park, S.Y. Hong, D.H. Chun, S.W. Kang, J.C. Park, D.-S. Lee, A highly susceptive mesoporous hematite microcube architecture for sustainable P-type formaldehyde gas sensors, Sens. Actuator B–Chem. 287 (2019) 437–444, https://doi.org/10.1016/j.snb.2019.01.153.

[5] Z. Tao, Z. Li, B. Zhang, G. Sun, M. Xiao, H. Bala, J. Cao, Z. Zhang, Y. Wang, Synthesis of urchin-like In₂O₃ hollow spheres for selective and quantitative detection of formaldehyde, Sens. Actuator B–Chem. 298 (2019), 126889, https://doi.org/10.1016/j.snb.2019.126889.

[6] X. Jiang, C. Li, Y. Chi, J. Yan, TG-FTIR study on urea-formaldehyde resin residue during pyrolysis and combustion, J. Hazard Mater. 173 (1–3) (2010) 205–210, https://doi.org/10.1016/j.jhazmat.2009.08.070.

[7] K. Huang, L. Kong, F. Yuan, C. Xie, In situ diffuse reflectance infrared Fourier transform spectroscopy study of formaldehyde adsorption and reactions on nano γ-Fe₂O₃ films, Appl. Surf. Sci. 270 (2013) 405–410, https://doi.org/10.1016/j.apsusc.2013.01.038.

[8] Y. Zhao, X. Zou, H. Chen, X. Chu, G.-D. Li, Tailoring energy level and surface basicity of metal oxide semiconductors by rare-earth incorporation for high-performance formaldehyde detection, Inorg. Chem. Front. 6 (2019) 1767–1774, https://doi.org/10.1039/c9qi00381a.

[9] H. Zhu, J. She, M. Zhou, X. Fan, Rapid and sensitive detection of formaldehyde using portable 2-dimensional gas chromatography equipped with photoionization detectors, Sens. Actuator B–Chem. 283 (2019) 182–187, https://doi.org/10.1016/j.snb.2018.11.156.

[10] Z. Han, Y. Qi, Z. Yang, H. Han, Y. Jiang, W. Du, X. Zhang, J. Zhang, Z. Dai, L. Wu, C. Fletcher, Z. Wang, J. Liu, G. Lu, F. Wang, Recent advances and perspectives on constructing metal oxide semiconductor gas sensing materials for efficient formaldehyde detection, J. Mater. Chem. C 8 (2020) 13169–13188, https://doi.org/10.1039/d0tc03750h.

[11] X. Tang, Y. Bai, A. Duong, M.T. Smith, L. Li, L. Zhang, Formaldehyde in China: production, consumption, exposure levels, and health effects, Environ. Int. 35 (8) (2009) 1210–1224, https://doi.org/10.1016/j.envint.2009.06.002.

[12] E. Sennik, N. Kilinc, Z.Z. Ozturk, Electrical and VOC sensing properties of anatase and rutile TiO₂ nanotubes, J. Alloys Compd. 616 (2014) 89–96, https://doi.org/10.1016/j.jallcom.2014.07.097.

[13] D. Wang, K. Wan, M. Zhang, H. Li, P. Wang, X. Wang, J. Yang, Constructing hierarchical SnO₂ nanofiber/nanosheets for efficient formaldehyde detection, Sens. Actuator B–Chem. 283 (2019) 714–723, https://doi.org/10.1016/j.snb.2018.11.125.

[14] Z. Wang, R. Zhang, F. Gu, D. Han, Facile synthesis of In₂O₃ nanoparticles with high response to formaldehyde at low temperature, Int. J. Appl. Ceram. Technol. 16 (4) (2019) 1570–1580, https://doi.org/10.1111/ijac.13244.

[15] X. Lai, G. Shen, P. Xue, B. Yan, H. Wang, P. Li, W. Xia, J. Fang, Ordered mesoporous NiO with thin pore walls and its enhanced sensing performance for formaldehyde, Nanoscale 7 (2015) 4005–4012, https://doi.org/10.1039/c4nr05772d.

[16] L. Guo, N. Xie, C. Wang, X. Kou, M. Ding, H. Zhang, Y. Sun, H. Song, Y. Wang, G. Lu, Enhanced hydrogen sulfide sensing properties of Pt-functionalized α-Fe₂O₃ nanowires prepared by one-step electrospinning, Sens. Actuator B–Chem. 255 (2018) 1015–1023, https://doi.org/10.1016/j.snb.2017.07.055.

[17] J. Zhang, J. Guo, H. Xu, B. Cao, Reactive-template fabrication of porous SnO₂ nanotubes and their remarkable gas-sensing performance, ACS Appl. Mater. Interfaces 5 (16) (2013) 7893–7898, https://doi.org/10.1021/am4019884.

[18] S. Zhang, Y. Li, G. Sun, B. Zhang, Y. Wang, J. Cao, Z. Zhang, Enhanced methane sensing properties of porous NiO nanaosheets by decorating with SnO₂, Sens. Actuator B–Chem. 288 (2019) 373–382, https://doi.org/10.1016/j.snb.2019.03.024.

[19] A. Dey, Semiconductor metal oxide gas sensors: a review, Mater. Sci. Eng. B–Adv. Funct. Solid–State Mater. 229 (2018) 206–217, https://doi.org/10.1016/j.mseb.2017.12.036.

[20] X. Lai, D. Wang, N. Han, J. Du, J. Li, C. Xing, Y. Chen, X. Li, Ordered arrays of bead-chain-like In₂O₃ nanorods and their enhanced sensing performance for formaldehyde, Chem. Mater. 22 (10) (2010) 3033–3042, https://doi.org/10.1021/cm100181c.

[21] J.-L. Wang, Q.-G. Zhai, S.-N. Li, Y.-C. Jiang, M.-C. Hu, Mesoporous In₂O₃ materials prepared by solid-state thermolysis of indium-organic frameworks and their high HCHO-sensing performance, Inorg. Chem. Commun. 63 (2016) 48–52, https://doi.org/10.1016/j.inoche.2015.11.015.

[22] S. Zhang, P. Song, J. Li, J. Zhang, Z. Yang, Q. Wang, Facile approach to prepare hierarchical Au-loaded In₂O₃ porous nanocubes and their enhanced sensing performance towards formaldehyde, Sens. Actuator B–Chem. 241 (2017) 1130–1138, https://doi.org/10.1016/j.snb.2016.10.023.

[23] Y. Lin, W. Wei, Y. Li, F. Li, J. Zhou, D. Sun, Y. Chen, S. Ruan, Preparation of Pd nanoparticle-decorated hollow SnO₂ nanofibers and their enhanced formaldehyde sensing properties, J. Alloys Compd. 651 (2015) 690–698, https://doi.org/10.1016/j.jallcom.2015.08.174.

[24] X. Xing, X. Xiao, L. Wang, Y. Wang, Highly sensitive formaldehyde gas sensor based on hierarchically porous Ag-loaded ZnO heterojunction nanocomposites, Sens. Actuator B–Chem. 247 (2017) 797–806, https://doi.org/10.1016/j.snb.2017.03.077.

[25] C. Dong, X. Liu, X. Xiao, G. Chen, Y. Wang, I. Djerdj, Combustion synthesis of porous Pt-functionalized SnO₂ sheets for isopropanol gas detection with a significant enhancement in response, J. Mater. Chem. 2 (2014) 20089–20095, https://doi.org/10.1039/c4ta04251d.

[26] J. Liu, L. Zhang, J. Fan, B. Zhu, J. Yu, Triethylamine gas sensor based on Pt-functionalized hierarchical ZnO microspheres, Sens. Actuator B–Chem. 331 (2021), 129425, https://doi.org/10.1016/j.snb.2020.129425.

[27] S. Wang, B. Xiao, T. Yang, P. Wang, C. Xiao, Z. Li, R. Zhao, M. Zhang, Enhanced HCHO gas sensing properties by Ag-loaded sunflower-like In₂O₃ hierarchical nanostructures, J. Mater. Chem. 2 (2014) 6598–6604, https://doi.org/10.1039/c3ta15110g.

[28] C. Dong, X. Liu, B. Han, S. Deng, X. Xiao, Y. Wang, Nonaqueous synthesis of Ag-functionalized In₂O₃/ZnO nanocomposites for highly sensitive formaldehyde sensor, Sens. Actuator B–Chem. 224 (2016) 193–200, https://doi.org/10.1016/j.snb.2015.09.107.

[29] J. Zhang, H. Lu, L. Zhang, D. Leng, Y. Zhang, W. Wang, Y. Gao, H. Lu, J. Gao, G. Zhu, Z. Yang, C. Wang, Metal–organic framework-derived ZnO hollow nanocages functionalized with nanoscale Ag catalysts for enhanced ethanol sensing properties, Sens. Actuator B–Chem. 291 (2019) 458–469, https://doi.org/10.1016/j.snb.2019.04.058.

[30] Y. Jia, F. Li, K. Fan, L. Sun, Cu-based bimetallic electrocatalysts for CO₂ reduction, Adv. Powder Mater. 1 (1) (2022), 100012, https://doi.org/10.1016/j.apmate.2021.10.003.

[31] B. Fang, Z. Xing, D. Sun, Z. Li, W. Zhou, Hollow semiconductor photocatalysts for solar energy conversion, Adv. Powder Mater. 1 (2) (2022), 100021, https://doi.org/10.1016/j.apmate.2021.11.008.

[32] L. Yu, F. Li, J. Zhao, Z. Chen, Revisiting catalytic performance of supported metal dimers for oxygen reduction reaction via magnetic coupling from first principles, Adv. Powder Mater. 1 (3) (2022), 100031, https://doi.org/10.1016/j.apmate.2022.01.004.

[33] J. Bai, C. Wang, K. Liu, H. Wang, Y. Liu, H. Suo, X. Liang, C. Zhang, F. Liu, C. Wang, P. Sun, G. Lu, Enhanced gas sensing performance based on the PtCu octahedral alloy nanocrystals decorated SnO$_2$ nanoclusters, Sens. Actuator B–Chem. 330 (2021), 129375, https://doi.org/10.1016/j.snb.2020.129375.

[34] J. Bai, Y. Shi, W. Liang, C. Wang, Y. Liu, H. Wang, F. Liu, P. Sun, Y. Zhang, G. Lu, PtCu nanocrystals with crystalline control: twin defect-driven enhancement of acetone sensing, Sens. Actuator B–Chem. 354 (2022), 131210, https://doi.org/10.1016/j.snb.2021.131210.

[35] Y. Xiong, Y. Lin, X. Wang, Y. Zhao, J. Tian, Defect engineering on SnO$_2$ nanomaterials for enhanced gas sensing performances, Adv. Powder Mater. 1 (3) (2022), 100033, https://doi.org/10.1016/j.apmate.2022.02.001.

[36] T. Lu, T. Li, D. Shi, J. Sun, H. Pang, L. Xu, J. Yang, Y. Tang, In situ establishment of Co/MoS$_2$ heterostructures onto inverse opal-structured N,S-doped carbon hollow nanospheres: interfacial and architectural dual engineering for efficient hydrogen evolution reaction, SmartMat 2 (2021) 591–602, https://doi.org/10.1002/smm2.1063.

[37] J. Zhu, R. Yang, G. Zhang, Atomically thin transition metal dichalcogenides for the hydrogen evolution reaction, ChemPhys Mater. 1 (2) (2022) 102–111, https://doi.org/10.1016/j.chphma.2021.11.005.

[38] Z. Wang, C. Hou, Q. De, F. Gu, D. Han, One-step synthesis of Co-doped In$_2$O$_3$ nanorods for high response of formaldehyde sensor at low temperature, ACS Sens. 3 (2) (2018) 468–475, https://doi.org/10.1021/acssensors.7b00896.

[39] D. Han, P. Song, S. Zhang, H. Zhang, Q. Xu, Q. Wang, Enhanced methanol gas-sensing performance of Ce-doped In$_2$O$_3$ porous nanospheres prepared by hydrothermal method, Sens, Actuator B–Chem. 216 (2015) 488–496, https://doi.org/10.1016/j.snb.2015.04.083.

[40] J. Wu, Q. Huang, D. Zeng, S. Zhang, L. Yang, D. Xia, Z. Xiong, C. Xie, Al-doping induced formation of oxygen-vacancy for enhancing gas-sensing properties of SnO$_2$ NTs by electrospinning, Sens. Actuator B–Chem. 198 (2014) 62–69, https://doi.org/10.1016/j.snb.2014.03.012.

[41] Z. Lin, N. Li, Z. Chen, P. Fu, The effect of Ni doping concentration on the gas sensing properties of Ni doped SnO$_2$, Sens. Actuator B–Chem. 239 (2017) 501–510, https://doi.org/10.1016/j.snb.2016.08.053.

[42] J. Hu, T. Wang, Y. Wang, D. Huang, G. He, Y. Han, N. Hu, Y. Su, Z. Zhou, Y. Zhang, Z. Yang, Enhanced formaldehyde detection based on Ni doping of SnO$_2$ nanoparticles by one-step synthesis, Sens. Actuator B–Chem. 263 (2018) 120–128, https://doi.org/10.1016/j.snb.2018.02.035.

[43] K. Zhu, S. Ma, Y. Tie, Q. Zhang, W. Wang, S. Pei, X. Xu, Highly sensitive gas sensors based on Y-doped SnO$_2$ hierarchical flower-shaped nanostructures, J. Alloys Compd. 792 (2019) 938–944, https://doi.org/10.1016/j.jallcom.2019.04.102.

[44] C. Wang, X. Cui, J. Liu, X. Zhou, X. Cheng, P. Sun, X. Hu, X. Li, J. Zheng, G. Lu, Design of superior ethanol gas sensor based on Al-doped NiO nanorod-flowers, ACS Sens. 1 (2) (2016) 131–136, https://doi.org/10.1021/acssensors.5b00123.

[45] Y. Jin, Z. Zhang, H. Yang, P. Wang, C. Shen, T. Cheng, X. Huang, Q. Shao, Boosting hydrogen production with ultralow working voltage by selenium vacancy-enhanced ultrafine platinum–nickel nanowires, SmartMat 3 (2022) 130–141, https://doi.org/10.1002/smm2.1083.

[46] S. Rani, S.C. Roy, M.C. Bhatnagar, Effect of Fe doping on the gas sensing properties of nano-crystalline SnO$_2$ thin films, Sens. Actuator B–Chem. 122 (2007) 204–210, https://doi.org/10.1016/j.snb.2006.05.032.

[47] S. Singkammo, A. Wisitsoraat, C. Sriprachuabwong, A. Tuantranont, S. Phanichphant, C. Liewhiran, Electrolytically exfoliated graphene-loaded flame-made Ni-doped SnO$_2$ composite film for acetone sensing, ACS Appl. Mater. Interfaces 7 (5) (2015) 3077–3092, https://doi.org/10.1021/acsami.5b00161.

[48] G. Qiao, S. Wang, X. Wang, X. Chen, X. Wang, H. Cui, Preparation and corrosion protection performance of a pulse co-deposited Ni/Co/SiO$_2$ hydrophobic composite coating, ChemPhys Mater. 1 (2) (2022) 119–125, https://doi.org/10.1016/j.chphma.2021.11.002.

[49] K. Cao, E. Cao, Y. Zhang, W. Hao, L. Sun, H. Peng, The influence of nonstoichiometry on electrical transport and ethanol sensing characteristics for nanocrystalline LaFeO$_3$−sensors, Sens. Actuator B–Chem. 230 (2016) 592–599, https://doi.org/10.1016/j.snb.2016.02.096.

[50] A. Rao, H. Long, A. Harley-Trochimczyk, T. Pham, A. Zettl, C. Carraro, R. Maboudian, In situ localized growth of ordered metal oxide hollow sphere array on microheater platform for sensitive, ultra-fast gas sensing, ACS Appl. Mater. Interfaces 9 (3) (2017) 2634–2641, https://doi.org/10.1021/acsami.6b12677.

[51] L. Soussi, T. Garmim, O. Karzazi, A. Rmili, A. El Bachiri, A. Louardi, H. Erguig, Effect of (Co, Fe, Ni) doping on structural, optical and electrical properties of sprayed SnO$_2$ thin film, Surface. Interfac. 19 (2020), 100467, https://doi.org/10.1016/j.surfin.2020.100467.

[52] M. Maaza, B.D. Ngom, M. Achouri, K. Manikandan, Functional nanostructured oxides, Vacuum 114 (2015) 172–187, https://doi.org/10.1016/j.vacuum.2014.12.023.

[53] B.D. Ngom, T. Mpahane, E. Manikandan, M. Maaza, ZnO nano-discs by lyophilization process: size effects on their intrinsic luminescence, J. Alloys Compd. 656 (2016) 758–763, https://doi.org/10.1016/j.jallcom.2015.09.230.

[54] Q. Liu, Y. Guo, Z. Chen, Z. Zhang, X. Fang, Constructing a novel ternary Fe(III)/graphene/g-C$_3$N$_4$ composite photocatalyst with enhanced visible-light driven photocatalytic activity via interfacial charge transfer effect, Appl. Catal. B Environ. 183 (2016) 231–241, https://doi.org/10.1016/j.apcatb.2015.10.054.

[55] S. Abdpour, E. Kowsari, M.R.A. Moghaddam, Synthesis of MIL-100(Fe)@MIL-53(Fe) as a novel hybrid photocatalyst and evaluation photocatalytic and photoelectrochemical performance under visible light irradiation, J. Solid State Chem. 262 (2018) 172–180, https://doi.org/10.1016/j.jssc.2018.03.018.

[56] D. Kong, H. Fan, D. Yin, D. Zhang, X. Pu, S. Yao, C. Su, AgFeO$_2$ nanoparticle/ZnIn$_2$S$_4$ microsphere p–n heterojunctions with hierarchical nanostructures for efficient visible-light-driven H$_2$ evolution, ACS Sustain. Chem. Eng. 9 (7) (2021) 2673–2683, https://doi.org/10.1021/acssuschemeng.0c07638.

[57] W. Guo, L. Huang, J. Zhang, Y. He, W. Zeng, Ni-doped SnO$_2$/g-C$_3$N$_4$ nanocomposite with enhanced gas sensing performance for the effective detection of acetone in diabetes diagnosis, Sens. Actuator B–Chem. 334 (2021), 129666, https://doi.org/10.1016/j.snb.2021.129666.

[58] Z. Li, J. Yi, Enhanced ethanol sensing of Ni-doped SnO$_2$ hollow spheres synthesized by a one-pot hydrothermal method, Sens. Actuator B–Chem. 243 (2017) 96–103, https://doi.org/10.1016/j.snb.2016.11.136.

[59] B. Liu, M. Wang, S. Liu, H. Zheng, H. Yang, The sensing reaction on the Ni-NiO (111) surface at atomic and molecule level and migration of electron, Sens. Actuator B–Chem. 273 (2018) 794–803, https://doi.org/10.1016/j.snb.2018.06.102.

[60] P.M. Bulemo, H.J. Cho, N.H. Kim, I.D. Kim, Mesoporous SnO$_2$ nanotubes via electrospinning-etching route: highly sensitive and selective detection of H$_2$S molecule, ACS Appl. Mater. Interfaces 9 (31) (2017) 26304–26313, https://doi.org/10.1021/acsami.7b05241.

[61] B. Liu, K. Li, Y. Luo, L. Gao, G. Duan, Sulfur spillover driven by charge transfer between AuPd alloys and SnO$_2$ allows high selectivity for dimethyl disulfide gas sensing, Chem. Eng. J. 420 (2021), 129881, https://doi.org/10.1016/j.cej.2021.129881.

[62] L.-Y. Zhu, K. Yuan, J.-G. Yang, H.-P. Ma, T. Wang, X.-M. Ji, J.-J. Feng, A. Devi, H.-L. Lu, Fabrication of heterostructured p-CuO/n-SnO$_2$ core-shell nanowires for enhanced sensitive and selective formaldehyde detection, Sens. Actuator B–Chem. 290 (2019) 233–241, https://doi.org/10.1016/j.snb.2019.03.092.

[63] X. Song, L. Li, X. Chen, Q. Xu, B. Song, Z. Pan, Y. Liu, F. Juan, F. Xu, B. Cao, Enhanced triethylamine sensing performance of α-Fe$_2$O$_3$ nanoparticle/ZnO nanorod heterostructures, Sens. Actuator B–Chem. 298 (2019), 126917, https://doi.org/10.1016/j.snb.2019.126917.

[64] Z. Song, H. Chen, S. Bao, Z. Xie, Q. Kuang, L. Zheng, Nanosheet-assembled, hollowed-out hierarchical γ-Fe$_2$O$_3$ microrods for high-performance gas sensing, J. Mater. Chem. 8 (2020) 3754–3762, https://doi.org/10.1039/c9ta12052a.

[65] Y. Wang, X. Meng, M. Yao, G. Sun, Z. Zhang, Enhanced CH$_4$ sensing properties of Pd modified ZnO nanosheets, Ceram. Int. 45 (10) (2019) 13150–13157, https://doi.org/10.1016/j.ceramint.2019.03.250.

[66] W. Liu, Y. Xie, T. Chen, Q. Lu, S. Ur Rehman, L. Zhu, Rationally designed mesoporous In$_2$O$_3$ nanofibers functionalized Pt catalysts for high-performance acetone gas sensors, Sens. Actuator B–Chem. 298 (2019), 126871, https://doi.org/10.1016/j.snb.2019.126871.

[67] Y.X. Li, Z. Guo, Y. Su, X.B. Jin, X.H. Tang, J.R. Huang, X.J. Huang, M.Q. Li, J.H. Liu, Hierarchical morphology-dependent gas-sensing performances of three-dimensional SnO$_2$ nanostructures, ACS Sens. 2 (1) (2017) 102–110, https://doi.org/10.1021/acssensors.6b00597.

[68] W. Tan, J. Tan, L. Li, M. Dun, X. Huang, Nanosheets-assembled hollowed-out hierarchical Co$_3$O$_4$ microrods for fast response/recovery gas sensor, Sens. Actuator B–Chem. 249 (2017) 66–75, https://doi.org/10.1016/j.snb.2017.04.068.

[69] S.-J. Kim, S.-H. Lee, C. J Lee, Organic vapour sensing by current response of porous silicon layer, J. Phys. D Appl. Phys. 34 (24) (2001) 3505–3509, https://doi.org/10.1088/0022-3727/34/24/314.

[70] L. Zhang, Y. Yin, Hierarchically mesoporous $SnO_2$ nanosheets: hydrothermal synthesis and highly ethanol-sensitive properties operated at low temperature, Sens. Actuator B–Chem. 185 (2013) 594–601, https://doi.org/10.1016/j.snb.2013.05.068.

[71] A. Montazeri, F. Jamali-Sheini, Enhanced ethanol gas-sensing performance of Pb-doped $In_2O_3$ nanostructures prepared by sonochemical method, Sens. Actuator B–Chem. 242 (2017) 778–791, https://doi.org/10.1016/j.snb.2016.09.181.

[72] X. San, G. Zhao, G. Wang, Y. Shen, D. Meng, Y. Zhang, F. Meng, Assembly of 3D flower-like NiO hierarchical architectures by 2D nanosheets: synthesis and their sensing properties to formaldehyde, RSC Adv. 7 (2017) 3540–3549, https://doi.org/10.1039/c6ra25883b.

[73] S. Zhang, P. Song, H. Yan, Q. Wang, Self-assembled hierarchical Au-loaded $In_2O_3$ hollow microspheres with superior ethanol sensing properties, Sens. Actuator B–Chem. 231 (2016) 245–255, https://doi.org/10.1016/j.snb.2016.03.020.

[74] S. Tian, X. Ding, D. Zeng, S. Zhang, C. Xie, Pore-size-dependent sensing property of hierarchical $SnO_2$ mesoporous microfibers as formaldehyde sensors, Sens. Actuator B–Chem. 186 (2013) 640–647, https://doi.org/10.1016/j.snb.2013.06.073.

[75] X. Zhang, W. Lan, J. Xu, Y. Luo, J. Pan, C. Liao, L. Yang, W. Tan, X. Huang, ZIF-8 derived hierarchical hollow ZnO nanocages with quantum dots for sensitive ethanol gas detection, Sens. Actuator B–Chem. 289 (2019) 144–152, https://doi.org/10.1016/j.snb.2019.03.090.

[76] W. Yang, P. Wan, X. Zhou, J. Hu, Y. Guan, L. Feng, Self-assembled $In_2O_3$ truncated octahedron string and its sensing properties for formaldehyde, Sens. Actuator B–Chem. 201 (2014) 228–233, https://doi.org/10.1016/j.snb.2014.05.003.

[77] F. Gu, C. Li, D. Han, Z. Wang, Manipulating the defect structure ($V_O$) of $In_2O_3$ nanoparticles for enhancement of formaldehyde detection, ACS Appl. Mater. Interfaces 10 (1) (2018) 933–942, https://doi.org/10.1021/acsami.7b16832.

[78] H.-J. Kim, K.-I. Choi, K.-M. Kim, C.W. Na, J.-H. Lee, Highly sensitive $C_2H_5OH$ sensors using Fe-doped NiO hollow spheres, Sens. Actuator B–Chem. 171–172 (2012) 1029–1037, https://doi.org/10.1016/j.snb.2012.06.029.